







Efficient CO₂ electroreduction on facet-selective copper films with high conversion rate

Gong Zhang ^{1,2,3,7}, Zhi-Jian Zhao ^{1,2,3,7}, Dongfang Cheng ^{1,2,3}, Huimin Li^{1,2,3}, Jia Yu^{1,2,3}, Qingzhen Wang^{1,2,3}, Hui Gao^{1,2,3}, Jinyu Guo⁴, Huaiyuan Wang^{1,2,3}, Geoffrey A. Ozin ⁵, Tuo Wang ^{1,2,3}✉ & Jinlong Gong ^{1,2,3,6}✉

Tuning the facet exposure of Cu could promote the multi-carbon (C₂+) products formation in electrocatalytic CO₂ reduction. Here we report the design and realization of a dynamic deposition-etch-bombardment method for Cu(100) facets control without using capping agents and polymer binders. The synthesized Cu(100)-rich films lead to a high Faradaic efficiency of 86.5% and a full-cell electricity conversion efficiency of 36.5% towards C₂+ products in a flow cell. By further scaling up the electrode into a 25 cm² membrane electrode assembly system, the overall current can ramp up to 12 A while achieving a single-pass yield of 13.2% for C₂+ products. An insight into the influence of Cu facets exposure on intermediates is provided by in situ spectroscopic methods supported by theoretical calculations. The collected information will enable the precise design of CO₂ reduction reactions to obtain desired products, a step towards future industrial CO₂ refineries.

¹School of Chemical Engineering and Technology, Tianjin University, Tianjin, China. ²Key Laboratory for Green Chemical Technology of Ministry of Education, Tianjin University, Tianjin, China. ³Collaborative Innovation Center of Chemical Science and Engineering (Tianjin), Tianjin, China. ⁴Department of Chemical Engineering, Stanford University, Stanford, CA, USA. ⁵Department of Chemistry, University of Toronto, 80 St. George Street, Toronto, ON, Canada. ⁶Joint School of National University of Singapore and Tianjin University, International Campus of Tianjin University, Binhai New City, Fuzhou, China. ⁷These authors contributed equally: Gong Zhang, Zhi-Jian Zhao. ✉email: wangtuo@tju.edu.cn; jlgong@tju.edu.cn

The renewable electricity-powered CO₂ reduction has been considered as one promising route to the product of chemical feedstocks, which might close the carbon loop^{1,2}. Multi-carbon (C₂+) products such as ethylene, ethanol, n-propanol, etc. are important raw materials in the chemical industry or can be used directly as fuels, thus the efficient CO₂ reduction to C₂+ products system is essential to the production of high-value commodity chemicals with a net negative carbon emissions footprint. Among various CO₂ reduction catalyst materials, Cu has been studied extensively as it can produce C₂+ products with appreciable selectivity³. Among numerous ways to promote C₂+ formation^{4–8}, adjusting the facet of Cu-based catalysts is an effective method since the dimerization reaction is facet sensitive⁹. According to the theoretical calculations, the Cu(100) facet can significantly lower the dimerization energy barrier¹⁰. Thus, it is an effective approach to improve the selectivity toward C₂+ by designing Cu catalysts with Cu(100) as the dominant exposed facet¹⁰. Colloidal chemistry is an inexpensive, simple, and widely used method for facet exposure control. It produces catalysts with preferential exposure of specific facets by using capping agents to manipulate surface energies, which changes the growth rates of different facets to alter the shape of nanocatalysts^{11,12}. Recently, colloiddally synthesized Cu nanocubes rich in Cu(100) facets were shown to achieve a Faradaic efficiency (F.E.) of ~57% towards ethylene¹³. However, the corresponding electricity conversion efficiency (E.C.E.) and single-pass yield have been rarely reported. Some studies also propose that the intermediates along the CO₂ reduction pathways can control the formation of specific facets, where the adsorption of the intermediates plays a role analogous to that of capping agents^{14,15}. Nonetheless, these approaches require specific chemicals, such as capping agents, to be selectively adsorbed on particular facets to reduce the surface energy^{11,12}. However, the effectiveness of the colloidal method might compromise to some extent since low-index facets of fcc transition metals often possess similar surface energies (1.25 J cm⁻² for Cu(111) and 1.43 J cm⁻² for Cu(100))^{15,16}. Besides, residual capping agents left on the catalyst surface could block catalytically active sites^{17,18}. Moreover, the colloiddally synthesized catalyst needs to be dispersed in a solution containing polymer binders (such as Nafion) to form a well-mixed ink before being drop-casted on the conductive support to form an electrode, which is not always compatible with the catalytic electrode system due to agglomeration and the peeling-off of catalysts especially when scaling up the electrodes^{19,20}. At the same time, due to the existence of the cross-linked network formed by polymer binders²¹, the contact between the colloiddally synthesized catalyst and the conductive substrate is weak^{22,23}, and plenty of active sites are further encapsulated²⁰, which will lead to slow electron transfer and low E.C.E. Thus, it is highly desirable to develop a novel approach to replace colloidal synthesis to prepare Cu electrodes with dominant (100) facets in one-step without using capping agents and polymer binders to achieve a high E.C.E. and a single-pass yield.

In this work, we describe the design and realization of a dynamic deposition-etch-bombardment process to produce Cu(100)-rich films as the CO₂ reduction electrode in one-step, which could break the limitation of using capping agents while avoiding the issue of catalyst loading faced by conventional methods. This Cu(100)-rich film yields a full-cell electricity conversion efficiency of 40.5% towards C₂+ products in the 4 cm²-membrane electrode assemble (MEA) system. This facile one-step method also makes it easier for scaling up electrodes, with a 25 cm² electrode exhibiting a 13.2% single-pass yield of C₂+ product at a total current of 12 A in the MEA system. Thanks to the controllable structure, the influence of facets on the adsorption and activation of intermediates is further revealed

by in situ spectroscopy and density functional theory (DFT) calculation.

Results

To amplify, when Cu atoms with high kinetic energy bombard the deposited Cu film, the high local temperature causes dynamic recrystallization^{24,25}. Facets with the relatively loose atomic arrangement, like Cu(100) (Supplementary Fig. 1c), would receive less damage and remain at lower temperatures thereby acting as recrystallization centers^{26,27}. As a result, the Cu(100) will preferentially grow, replacing the more densely packed Cu(111) facet (Supplementary Fig. 1b). Therefore, by controlling the kinetic energy of bombarding copper atoms, the exposure ratio of Cu(100) facets could be adjusted.

To realize the simultaneous deposition, etching, and bombardment, high-energy radio frequency (RF) sputtering was adopted to prepare Cu(100)-rich films (details in the “Methods”), which enables the direct deposition of catalysts on carbon-based gas diffusion layers (GDLs) as electrodes in one-step (Supplementary Fig. 1a). Three typical types of sputtered Cu films with different Cu(100) proportions were obtained by adjusting the RF power to control the kinetic energy (E_k) of the bombarding Cu atoms (Fig. 1a, details in “Methods”), resulting in low-power, medium-power, and high-power sputtered Cu films (denoted as LS-Cu, MS-Cu, HS-Cu, respectively). The obtained HS-Cu film is prone to expose the Cu(100) facet, as evidenced by transmission electron microscopy (TEM, Supplementary Fig. 2a) and X-ray diffraction (XRD, Supplementary Fig. 3a), while LS-Cu tends to form Cu(111) facet (Supplementary Figs. 2c and 3a). The energy of Cu atoms generated by thermal evaporation² or low-rate sputtering process^{4,28} is usually not high enough, rendering Cu films that favor the Cu(111) facet exposure similar to LS-Cu. As different Cu facets feature distinctive OH⁻ electrochemical adsorption behaviors^{29,30}, surface structures of these samples were probed by using the OH⁻ electroadsorption technique (the features were labeled by comparing the CVs to those of single crystals shown in Supplementary Fig. 4)³¹. The cyclic voltammograms (CVs) of OH_{ads} peaks (Supplementary Fig. 3b) reveal that the presence of Cu(111) is suppressed in the HS-Cu film. Therefore, this deposition-etch-bombardment process successfully realizes the replacement of Cu(100) to Cu(111) facets, adjusting the facet exposure of Cu.

However, these obtained Cu films (i.e. LS-Cu, MS-Cu, HS-Cu) lack a large electrochemically active surface area (ECSA, Supplementary Fig. 26 and Supplementary Table 1) to realize high-rate CO₂ electrolysis³². To increase the ECSA, an oxidation–reduction procedure was included, during which the preferential exposure of Cu(100) could be maintained. Specifically, molecular O₂ (with a constant partial pressure of 0.67 Pa) was introduced during this deposition-etch-bombardment process to obtain Cu₂O as precatalysts, which could be further reduced during the pre-reduction process (–0.5 V vs. the RHE) under the same CO₂ reduction conditions to metallic Cu with the Cu(100) facets retained (Fig. 1a, details in “Methods”). The same crystallographic relationship exists between the oxidation and reduction processes for Cu(100)/(111) and Cu₂O(100)/(111)^{10,33}, since oxygen atoms could pack into the interlayer sites of different planes of Cu, causing a lattice expansion while retaining the underlying fcc crystal structure with the inclusion of oxygen³³. Therefore, the introduction of an oxidation–reduction step will be able to increase the ECSA while retaining the same Cu(100) exposure. Correspondingly, samples obtained by reactive sputtering followed by reduction are referred to as low-power, medium-power, and high-power reactively sputtered Cu films followed by reduction (denoted as LRS-Cu, MRS-Cu, and HRS-Cu). Typical XRD patterns (Supplementary Fig. 5a) show

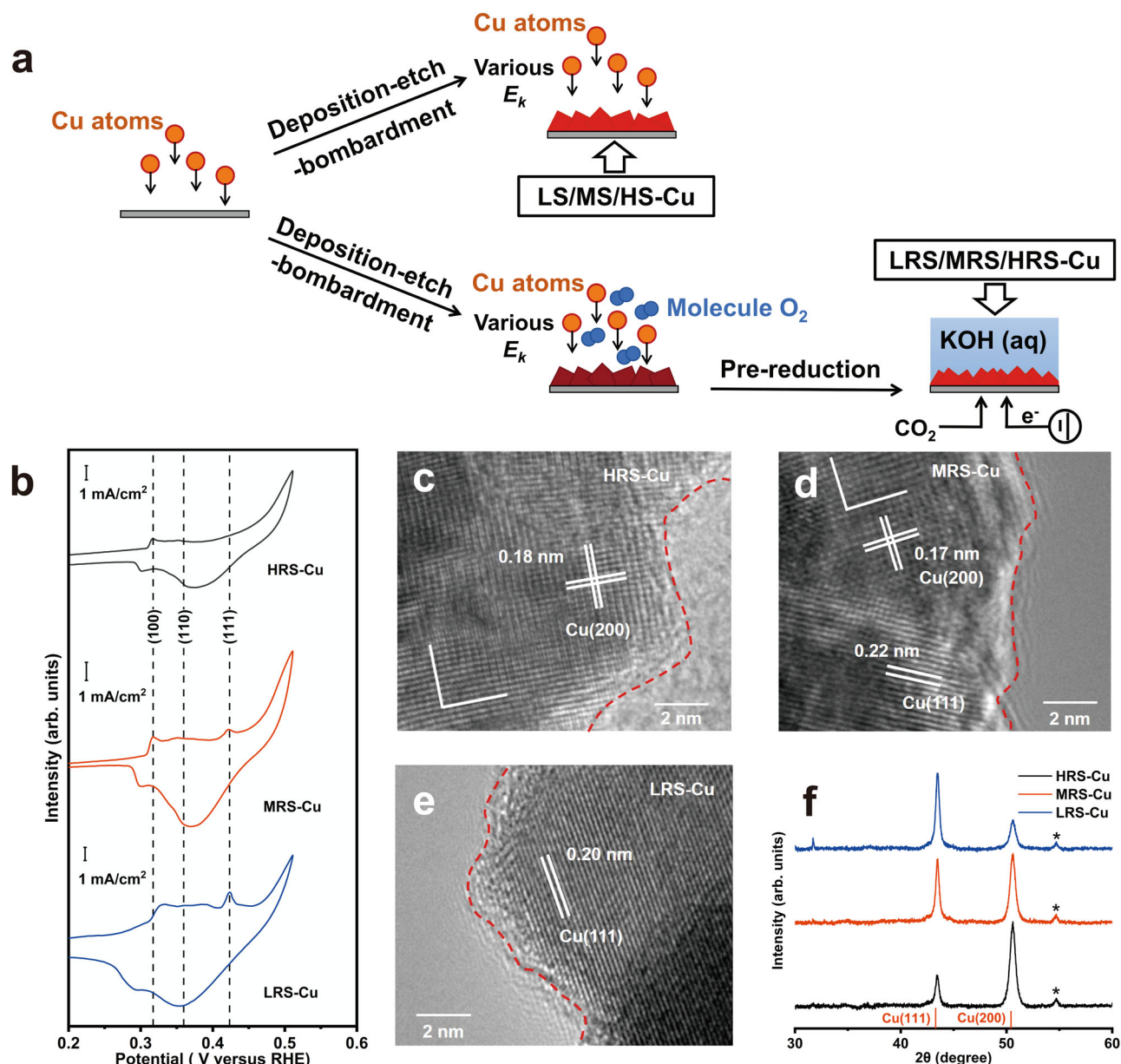


Fig. 1 characterization of various Cu films. **a** A schematic illustration of the synthesis process for LS/MS/HS-Cu and LRS/MRS/HRS-Cu. **b** Voltammograms of resulting electrodes collected immediately after pre-reduction. Typical TEM images of **c** HRS-Cu, **d** MRS-Cu, and **e** LRS-Cu. **f** Typical XRD patterns of resulting electrodes. As visual aids, the red dash line indicates the surfaces of the resulting electrodes. The precatalysts of HRS/MRS/LRS-Cu were pre-reduced under -0.5 V versus the RHE for 1 h, and the other conditions of prereluction are the same as that of the CO_2 reduction. The labeling of Cu(200) is used for easier comparison with XRD, in which only (200), the second-order diffraction of (100) could be detected. The peaks marked with an asterisk in XRD patterns originate from carbon-based GDL substrate.

that all the obtained precatalysts are mainly Cu_2O , which is confirmed by X-ray photoelectron spectroscopy (XPS), Auger spectroscopy (Supplementary Fig. 5b, c), and Raman spectroscopy (Supplementary Fig. 4d). The same type of Cu facets distribution could be maintained for these electrodes regardless of the oxidation-reduction process according to TEM (Fig. 1c–e, more images of different samples are also provided in Supplementary Figs. 7–9) and XRD (Fig. 1f), consistent with previous reports^{10,34}. The different proportions of Cu(100) facet on these samples (i.e. HRS-Cu, MRS-Cu, and LRS-Cu) are also evidenced by the electrochemical OH^- adsorption peaks on Cu(100) and Cu(111) at potentials of ~ 0.33 and 0.43 V versus the RHE (Fig. 1b). Meanwhile, large ECSA is obtained for these samples (Supplementary Table 1). Thus, this one-step surfactant-free route indeed leads to nanostructured Cu

films with preferred Cu(100) exposure and high surface area that could be further used as CO_2 reduction electrodes.

To further explore the importance of the high-energy atom bombardment proposed above, another control electrode was prepared. Cu_2O precatalyst (Supplementary Fig. 10) was obtained through wet chemistry without using capping agents (denoted as W-Cu). Then this control Cu_2O precatalyst was airbrushed onto GDEs and pre-reduced to Cu under CO_2 reduction conditions to form a control electrode (details in “Methods”). The typical TEM image shows that the lattice fringes corresponding to Cu(111) are widely distributed in this control electrode (Supplementary Fig. 11a)³². These observations are in good agreement with the XRD pattern (Supplementary Fig. 11b) and CV of OH_{ads} peaks (Supplementary Fig. 11c). It is also worth noting that LRS-Cu,

MRS-Cu, HRS-Cu, and W-Cu all consist of metallic Cu only without residual oxides after the pre-reduction, as confirmed by in-situ Raman spectroscopy (Supplementary Fig. 12, details in “Methods”). Thus, this control experiment reveals that the lack of high-energy atom bombardment during the synthesis process would result in the dominant exposure of Cu(111) facets, similar to the scenario of lacking capping agents that are widely used in the synthesis of Cu nanocubes^{34,35}.

Before performance testing, it was confirmed that different samples (LRS-Cu, MRS-Cu, HRS-Cu, and W-Cu) possess similar mass loadings (Supplementary Table 2), catalyst layer thickness (Supplementary Fig. 13) and morphology (Supplementary Fig. 14) of Cu, which ensures a fair comparison to explore the activity difference among various samples^{36–39}. The activities were evaluated at different potentials using 2 M KOH (aq.) as the electrolyte (Fig. 2a and Supplementary Figs. 16–19, details in “Methods”) in a flow cell electrolyzer (Supplementary Fig. 15) for CO₂ reduction with an effective electrode geometric area of ~0.64 cm² for both cathode and anode. As for HRS-Cu, the products detected in significant quantities were ethylene, ethanol, n-propanol, and CO. At more negative potentials, a small amount of methane was produced, and the remaining charge was attributed to the competing hydrogen evolution reaction (Fig. 2b). Compared with the control samples, the HRS-Cu exhibits a maximum F.E. of 58.6% for ethylene, 86.6% for C₂+ products (containing ethylene). Consistently, the HRS-Cu sample also exhibits the largest ethylene and C₂+ products partial current densities (Fig. 2c, d and Supplementary Fig. 17c, d) among the four samples at all applied potentials. Moreover, at the applied potential of –0.85 V versus the RHE, the C₂+ to C₁ ratio of the HRS-Cu electrode reaches about 15.2, which largely outperforms that of its counterparts (Supplementary Fig. 18). Due to the close contact between the catalytic Cu film and the GDL substrate, the reaction system could exhibit higher E.C.E. The corresponding full-cell E.C.E. towards ethylene and C₂+ products of this HRS-Cu-based reaction system reaches 24.8 and 36.5%, respectively, exceeding the efficiency of many other reaction systems reported so far (see below). The stability of the HRS-Cu was also examined under a constant applied potential of –0.75 V versus the RHE for 4.5 h (270 min), where ethylene and C₂+ F.E.s remained stable over the test duration (Fig. 2e and Supplementary Fig. 19). Although the surface of the Cu-based catalysts may undergo reconstruction during the reaction to obtain Cu(100)⁴⁰, the HRS-Cu, MRS-Cu, and LRS-Cu samples after use show similar surface exposures as before the reaction (Supplementary Figs. 20–22), indicating that the reconstruction process could not significantly change the main facet exposure, and thus surface reconstruction alone cannot guarantee electrodes similar to the HRS-Cu (showing a predominant Cu(100) exposure without undergoing reconstruction). The mass of the HRS-Cu sample after the reaction is also almost the same as that before the reaction (Supplementary Table 3), which further indicates that the firm conjunction between the substrate and the active composition. If the hydrophobicity of GDLs can be further improved² and the reaction rate of carbonate formation can be reduced⁴¹, the stability of the sample in the flow cell will be longer.

To examine the influence of Cu(100) exposure over C₂+ products formation in CO₂ reduction, Tafel analyses (Supplementary Fig. 23) were conducted on various samples. It is clear that C₂+ products formation depends strongly on the surface structure. With the increasing exposure of Cu(100) facets, a lower change of the Tafel slope can be observed, which indicates that the Cu(100) surface is beneficial to the formation of C₂+ products. However, the Tafel slope of all samples locates at approximately 120–140 mV dec^{–1}, implying that they might share the same rate-determining step (details in “Methods”),

which is further validated by the results of CO partial pressure dependence experiments (Supplementary Figs. 24, 25). To further compare the reaction rates, the performances are normalized to the ECSA (details in “Methods”). Obviously, the current densities of specific ethylene and C₂+ products of HRS-Cu are larger than other electrodes (Supplementary Fig. 27), which indicates the highest intrinsic activities of HRS-Cu.

Understanding the behaviors of adsorbates is essential to the inquiry into the nature of the catalytic activity. Thus, in-situ attenuated total reflectance (ATR)-surface-enhanced infrared absorption spectroscopy (ATR-SEIRAS, details in “Methods”) was applied to investigate the effect of facets exposure on the adsorption of intermediates. When the potential is swept from –0.1 to –1.5 V versus the RHE, a positive band centered at ~2050 cm^{–1} which corresponds to the linear-bond CO (CO_L, a reactive adsorbed species) is observed on all electrodes (Fig. 3a–c and Supplementary Fig. 28)^{42–44}. Meanwhile, a small positive band centered at ~1800 cm^{–1}, which corresponds to the bridge-bond CO (CO_B, an unreactive adsorbed species)⁴⁴ is also observed on the surface of other samples except the HRS-Cu. These results of the ATR-SEIRAS are also corroborated by the corresponding Raman spectra, where the HRS-Cu surface was covered by abundant CO_L^{45,46}, while the LRS-Cu surface exhibited a pronounced appearance of CO_B (Supplementary Fig. 30). The appearance of CO_B might result from the interconversion of CO_L. According to the literature, when the *CO (*denotes the adsorbed species) coverage of the electrode decreases, a fraction of CO_L would convert to CO_B⁴⁴. Therefore, the increase of CO_B ratio reveals the reduction of surface *CO coverage. By calculating the CO_B to CO_L ratio of different samples, the *CO coverage might decrease as the exposure of Cu(100) facets decreases (Supplementary Fig. 29). Normally, *H and *CO occupy most of the surface sites, so they are in direct competition with each other for surface sites. Meanwhile, the surface coverage of *CO eventually influences the distribution of products derived from CO₂ reduction. It has been previously speculated that when the surface cannot maintain a high *CO coverage, the corresponding *H coverage will increase, inhibiting the dimerization of *CO to produce C₂+ products, thereby shifting the selectivity to C₁ products and H₂^{47–49}, which is also demonstrated by the results of our CO partial pressure dependence experiments (Supplementary Figs. 24, 25). Meanwhile, the results of CO₂ reduction performance support the above speculation. The LRS-Cu and the W-Cu with a lower exposure of Cu(100) facets exhibit the highest F.E. of methane, meanwhile, the methane F.E. increases rapidly as the potential becomes negative (Supplementary Fig. 31). Thus, these ATR-SEIRAS results prove that Cu(100) facet might be a type of strong *CO adsorption site, and a higher exposure of Cu(100) facets is beneficial to the increase of strong adsorption sites on the surface that maintains a higher *CO coverage on the surface, thereby leading to the catalyst with a higher C–C coupling performance, which is also supported by other experimental and computational studies^{50–52}.

Since the ATR-SEIRAS cannot directly provide the adsorption energy and activation barrier of the intermediate, DFT calculations on Cu(111) and Cu(100) (3×3) models were performed to further understand the facet exposure effect (Supplementary Fig. 32, details in “Methods”). Based on the Tafel analysis and CO partial pressure dependence study (Supplementary Figs. 23, 24), the energetics of *OCCO formation is chosen as the main consideration. Previous work has found that the solvent and cation effects can stabilize *COCO, hence an appropriate electrochemical interface was built up to explore the mechanism of this dimerization procedure (Fig. 3d and Supplementary Figs. 34–36)⁵³.

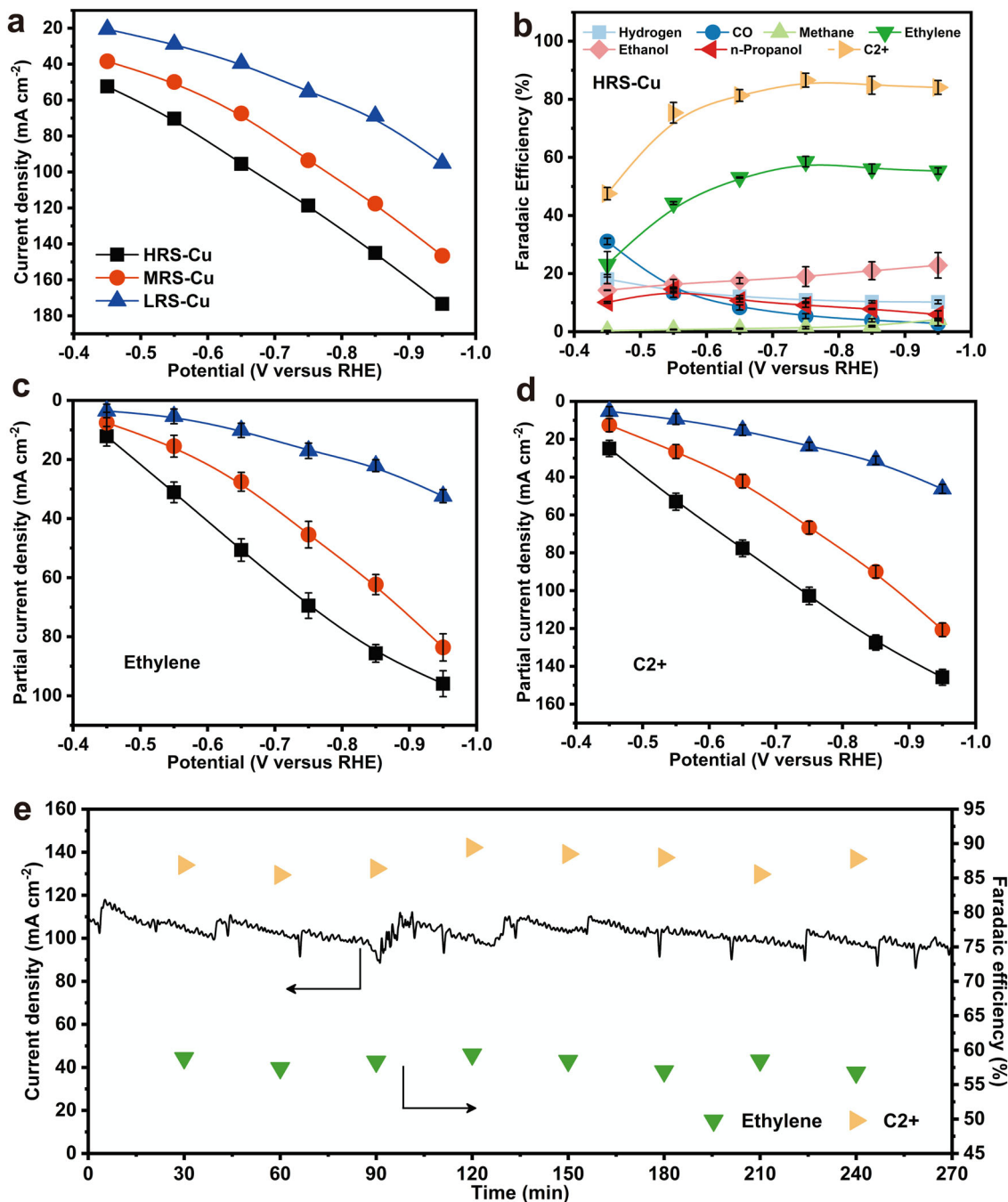


Fig. 2 Catalytic performance of various Cu films. **a** Current–voltage (*I*–*V*) curves on various electrodes measured in CO₂-flowed 2 M KOH electrolytes. **b** Faradaic efficiencies of CO₂ reduction products on the HRS-Cu sample as a function of different applied potentials. **c** Ethylene and **d** C₂⁺ products partial current densities obtained on various samples at different applied potentials. **e** Stability test over a span of 4.5 h (270 min) of CO₂- electrolysis in 2 M KOH (aq.) at –0.75 V versus the RHE. The oscillation of the current density is due to the repeated release of O₂ bubbles in the anode side of the flow cell. C₂⁺ products include ethylene, ethanol, and n-propanol. Error bars represent the standard deviation from at least three independent measurements.

From the DFT calculation results, the binding of *CO is the weakest on the Cu(111) facet (Supplementary Fig. 33), which is not suitable to build up a sufficient coverage of *CO on the surface to promote the kinetics of C–C coupling. Therefore, LRS-Cu and W-Cu would shorten the *CO stay and reduce the *CO coverage as compared to HRS-Cu, leading to a higher CO F.E. (Supplementary Fig. 16). In addition, the barriers of various C–C coupling processes are always higher on the Cu(111) facet than on Cu(100) facet, implying that *CO dimerization is the most sluggish step on the Cu(111) facet (Fig. 3e). Thus, LRS-Cu and W-Cu are less active in catalyzing the reduction of CO₂ to C₂⁺

products. These theoretical calculations are in good agreement with our ATR-SEIRAS and performance test results.

Due to the impressive E.C.E of this HRS-Cu-based reaction system, a PV-EC system (Fig. 4a) was further constructed to demonstrate the photosynthesis of C₂⁺ products. Using the same test conditions (electrolyzer, cathode, anode, and electrolyte, details in “Methods”) for measuring the CO₂ reduction performance on the cathode side (as in Fig. 2), it is found that an overall cell voltage of about 2.5 V is required (Fig. 4b) to obtain an operating current density varying from 60 to 70 mA cm⁻² (Fig. 2a), which could be translated to a cathodic potential of ~

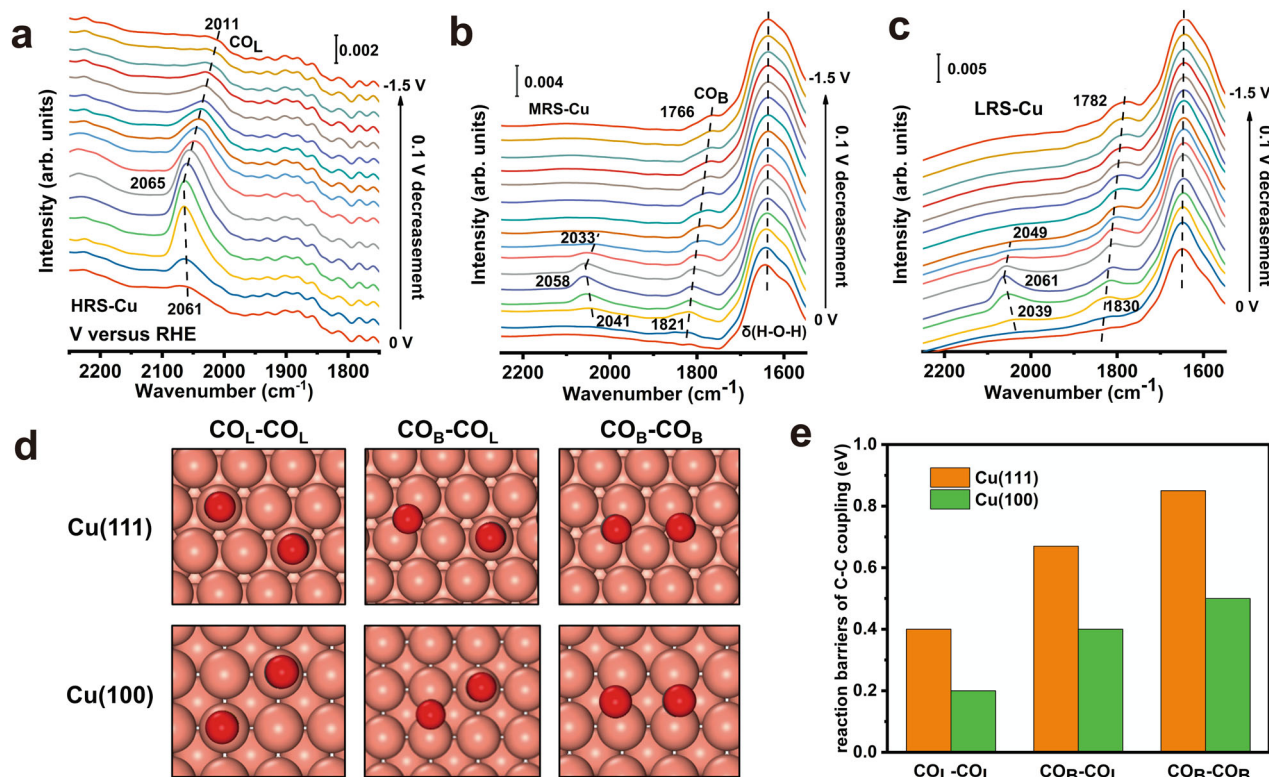


Fig. 3 Spectroscopic investigations of various Cu films and DFT calculations on different Cu facets. In situ ATR-SEIRAS spectra of **a** HRS-Cu; **b** MRS-Cu; **c** LRS-Cu; **d** adsorption geometry for different C–C coupling precursors (i.e., $\text{CO}_L\text{-CO}_L$, $\text{CO}_B\text{-CO}_L$, $\text{CO}_B\text{-CO}_B$), where solvent molecules are not presented to show the adsorbate configurations; **e** reaction barriers for C–C coupling from different precursors on Cu(100) and Cu(111) facets.

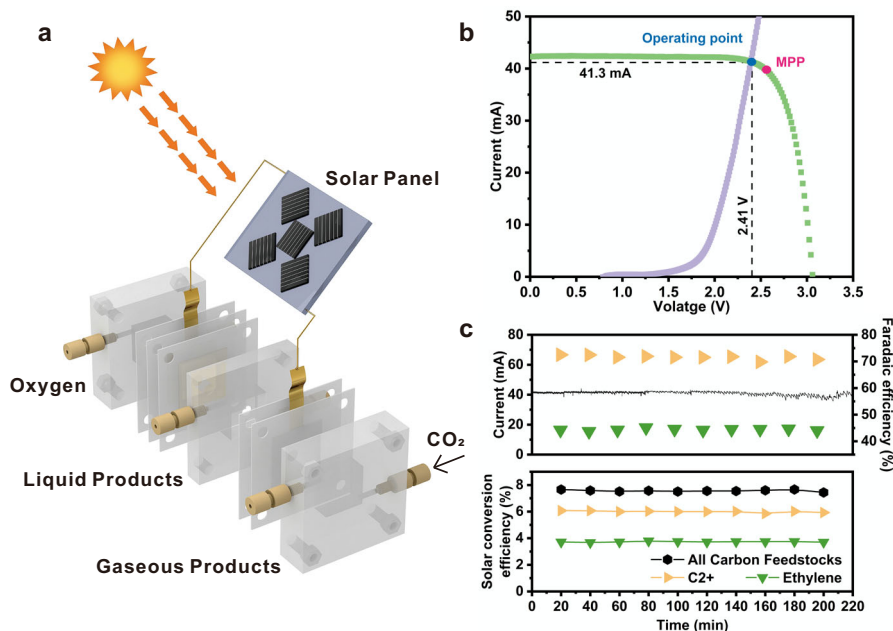


Fig. 4 Solar-powered CO_2 reduction. **a** Schematic of the PV-EC system. **b** Photovoltaic and electrocatalytic I–V behaviors. The photovoltaic performance is shown under light (green) with the MPP marked by a red dot. The measured operating current of the CO_2 electrolysis system (cathode, anode, and anion exchange membrane) at different voltages has been marked by the purple curve. The observed long-term operating point is marked by a blue dot, with the black dashed lines showing the corresponding current and voltage. **c** Faradaic efficiency towards ethylene and C_2^+ products, solar current, and solar conversion efficiency as a function of reaction time. Carbon feedstocks include CO, methane, ethylene, ethanol, and n-propanol. C_2^+ products include ethylene, ethanol, and n-propanol.

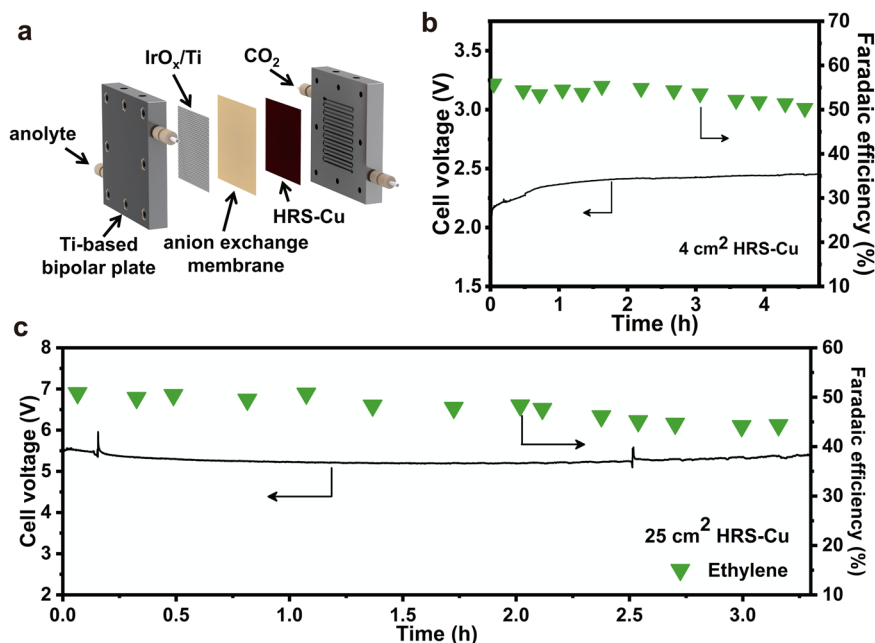


Fig. 5 Scaling up the CO₂ reduction system. **a** Schematic of the MEA system. The gaskets are not shown. **b** Stability test over a span of ~4.5 h of CO₂-electrolysis in a 4 cm²-MEA system at the total current density of 120 mA cm⁻². **c** Stability test over a span of ~3.5 h of CO₂-electrolysis in a 25 cm²-MEA system at the total current of 12 A. The decrease in ethylene F.E. and the increase in cell voltage may be attributed to the formation of carbonate on the cathode side and the cathode water flooding.

−0.55 V versus the RHE that yields ~45 and ~72% F.E. for ethylene and C₂+ products (containing ethylene), respectively (Fig. 2b). The deviation of these F.E.s from the maximized F.E.s for ethylene and C₂+ products is because of the matching between electrolyzer and the solar panel towards the maximum power point (MPP) of the solar panel. Considering that the effective area of the HRS-Cu sample is ~0.64 cm², the operating current varies from 38.4 to 44.8 mA. The widely available p–n⁺ solar cells, with an open circuit potential of ~0.6 V and a short-circuit current density of ~36 mA cm⁻², were selected and cut into ~1.14 cm² pieces. By connecting five of them in series, the solar panel would provide the suitable voltage and current for the CO₂ reduction electrolyzer near the MPP of the solar panel (i.e., the PV system). I–V curve of the obtained solar panel was measured under simulated AM 1.5G 1-sun illumination (Fig. 4b). This curve crosses the I–V curve of the electrolyzer at the point (i.e., the operating point) where its cathodic current and voltage are ~41.3 mA and ~2.41 V, respectively, which matches well with the MPP output metrics of the solar panel (39.8 mA at 2.53 V), indicating the optimum solar-to-electricity conversion process in our integrated device.

During ~3.7 h (220 min) of electrolysis powered by 1-sun solar illumination, the cathodic current of the electrolyzer was stable at ~41.3 mA and the F.E. of ethylene and C₂+ products stabilized at ~45 and ~72%, respectively (Fig. 4c and Supplementary Figs. 37–39). Although this selectivity is already deviated from the maximum F.E.s owing to MPP matching, such a PV-EC system still yields a solar-to-ethylene efficiency of ~4.0% and a solar-to-C₂+ products efficiency of ~6.0% (Fig. 4c) under simulated 1 Sun illumination, which exceeds the efficiency of general natural photosynthesis for producing carbohydrates (3–6%)⁵⁴. Such efficiency is also able to match a recent state-of-the-art perovskite solar cells-powered Cu–Ag bimetallic reaction system⁵⁵, while a longer stability and larger CO₂ reduction current are obtained in this system. The performance of this work also exceeds that of most previously reported copper-based PV-EC systems (Supplementary Table 4), which provides a benchmark for solar

conversion efficiency while using feasibly available Si-based solar cells and earth-abundant low-cost electrode materials.

The membrane electrode assemble system (MEA) was further adopted to scale up the CO₂ reduction system (Supplementary Fig. 40, details in “Methods”). On the cathode side, humidified CO₂ gas was supplied (Fig. 5a), which reduces the direct contact between the catalyst and the aqueous electrolyte, while reducing the ohmic resistance of the electrolyte^{56,57}. At the same time, the one-step deposition-etch-bombardment process proposed in this work is based on a widely used vacuum deposition process similar to the photovoltaic industries, thus its marginal cost for producing large-area electrodes can be largely reduced with mass production. In addition, this method does not require additional catalyst loading steps and does not use additional chemicals, accelerating the continuous preparation of large-area electrodes and avoiding potential electrode contamination. Therefore, the combination of a MEA reaction system and this preparation method is particularly suitable for the scale-up of CO₂ reduction.

The electrode area was enlarged to 4 cm², and the CO₂ reduction performance test was performed in the MEA system (the area of cathodic flow fields is 4 cm², referred as to the 4 cm²-MEA) at a current density of 120 mA cm⁻² corresponding to the maximum ethylene F.E. (58.6%) in the flow cell system (Fig. 5b). The optimal ethylene F.E. reaches 55.8%, while the corresponding full-cell E.C.E of ethylene and C₂+ products increase to 26.4 and 40.2%, respectively. After ~4.5 h of operation (Supplementary Fig. 41), the ethylene selectivity (50.4%) still remains above 90% of the initial value (55.8%). Although many works have obtained impressive CO₂ reduction selectivity, the single-pass yield for C₂+ products is generally low (mostly below 3%, Supplementary Table 5). In order to improve the single-pass yield of C₂+ products, it is vital to further increase the current density and electrode area without affecting the transport of CO₂ (details in the “Methods”). Using the one-step method proposed in this work, a HRS-Cu electrode with 25 cm² activity area could be easily fabricated with the deposition-etch-bombardment process (Supplementary Fig. 42). In a 25 cm² MEA system (i.e., the area

of cathodic flow fields is 25 cm^2), the optimal ethylene F.E. of HRS-Cu reached 50.9% and maintained above 45% (Fig. 5c and Supplementary Fig. 43) after $\sim 3.5 \text{ h}$ of operation at a total current of 12 A (i.e., 480 mA cm^{-2}). The corresponding single-pass yield of CO_2 towards C_2^+ products increased to and 13.2%, with ethylene increased to 12.0%. However, a corresponding decrease in E.C.E. was observed (Supplementary Table 5). Therefore, using more efficient anode materials, while controlling the operating conditions of the device such as temperature and pressure, or designing a new flow field structure to enhance CO_2 mass transfer may be effective ways to further improve the E.C.E.

Discussion

In conclusion, this work demonstrates a deposition-etch-bombardment process that feasibly increases the exposure of Cu(100) facets in low-cost nanostructured Cu films. This strategy obviates the use of capping agents, achieving precise control of surface structures in a one-step approach. The obtained Cu(100)-rich film functions as a high-performance electrode for CO_2 reduction towards ethylene and C_2^+ products. In flow cell, it realized ethylene and C_2^+ (containing ethylene) F.E.s of 58.6 and 86.6%, respectively. In addition, this deposition-etch-bombardment method bypasses the electrode assembly process, avoids the use of polymer binders, enhances the contact between the catalytic film and the substrate. Due to the above advantages, in flow cell, a corresponding full-cell E.C.E. of 24.8 and 36.5% for ethylene and C_2^+ products were obtained, respectively, which is a notable advance over existing single metallic Cu-based systems. Moreover, this preparation method is flexible and easy to achieve electrode scale-up. When a 4 cm^2 electrode was applied to the MEA system, the corresponding full-cell E.C.E. could be increased to 40.5 and 26.8%, respectively, without compromising product selectivity. When the electrode area of the MEA system is increased to 25 cm^2 , the single-pass yield of C_2^+ products can be further increased to 13.2%, with an ethylene yield of 12.0%. In situ ATR-SEIRAS studies and theoretical calculations provide insights into the role of Cu(100) facets for increasing $^*\text{CO}$ coverage and reducing the energy barrier of C–C coupling, vital for ethylene and C_2^+ products formation. The potential of using this Cu(100)-rich film for photosynthesis was also demonstrated using renewable electricity generated by Si solar panels, achieving a solar-to- C_2^+ products efficiency of $\sim 6.0\%$ under simulated 1 Sun illumination. Future research endeavors may focus on the generation of energetic particles (atoms, molecules, ions, etc.) in other environments such as solutions in ambient conditions, which may further reduce the cost of one-step facet control by this vacuum-based deposition-etch-bombardment method.

Methods

Synthesis of LS-Cu, MS-Cu, HS-Cu. The deposition-etch-bombardment process was conducted in a custom-designed radio frequency (RF, 13.56 MHz) magnetron sputtering system (Supplementary Fig. 1a). For LS-Cu, Ar was delivered into the system. The deposition chamber was pumped down by a mechanical pump and a molecular pump that resulted in a base pressure of $2.0 \times 10^{-4} \text{ Pa}$. The flow rate of Ar was set as 20 standard cubic centimeters per minute (sccm). During the deposition, the RF power was 40 W , and the working pressure was 4 Pa . The deposition time was 15 min . The target to substrate distance was set to 7 cm . Commercial GDLs were cut into squares ($5 \times 5 \text{ cm}$) for use as substrates. For MS-Cu, the RF power was set as 100 W and the deposition time was 7.5 min , other conditions were the same as LS-Cu. For HS-Cu, the RF power was set as 200 W and the deposition time was 3.5 min , other conditions were the same as LS-Cu.

Synthesis of LRS-Cu, MRS-Cu, and HRS-Cu. During the synthesis process of precatalysts of LRS-Cu, MRS-Cu, and HRS-Cu, O_2 was also introduced to the Ar atmosphere. The flow rates of Ar and O_2 were 20 and 4 sccm , respectively, to achieve a partial pressure of O_2 of 0.67 Pa . Other conditions were the same as those of LS-Cu, MS-Cu, and HS-Cu. The obtained precatalysts were pre-reduced at -0.5 V versus the RHE for 1 h under the same conditions as CO_2 electroreduction. Pre-reduction was carried out with a potentiostat (CompactStat.e20250, IVIUM).

After pre-reduction, the final samples (i.e., LRS-Cu, MRS-Cu, and HRS-Cu) were obtained.

Synthesis of W-Cu. The W-Cu was fabricated through the electrochemical pre-reduction of the Cu_2O nanorods at -0.5 V versus the RHE for 1 hour under the same conditions as CO_2 electroreduction. After pre-reduction, the electrode was directly used for CO_2 reduction. The Cu_2O nanorods were prepared by annealing the $\text{Cu}(\text{OH})_2$ nanorods in the Ar atmosphere at 500°C for 2 h with a heating rate of $10^\circ\text{C min}^{-1}$. The $\text{Cu}(\text{OH})_2$ nanorods were prepared by a previous method with some modifications³². The obtained Cu_2O nanorods were airbrushed onto the commercial GDLs at an approximate loading of 0.9 mg/cm^2 , measured through weighing GDLs before and after airbrushing. The catalyst ink was prepared by dispersing 200 mg of Cu_2O nanorods and $50 \mu\text{L}$ of Nafion Solution (Sigma-Aldrich) in $750 \mu\text{L}$ isopropyl alcohol and $250 \mu\text{L}$ of ultra-purity water ($18.2 \text{ M}\Omega \text{ cm}$) and sonicated for 1 h before airbrushing (H-SET, Paasche). Pre-reduction was carried out with a potentiostat (CompactStat.e20250, IVIUM).

Characterizations. Field-emission scanning electron microscopy (FESEM) (Hitachi S-4800, 3 kV) was used to characterize the morphology and microstructure of the samples. Transmission electron microscopy (TEM), High-resolution TEM (HRTEM) images were obtained at 200 kV (JEOL JEM-2100F). The crystal structure was determined by X-ray Diffractometer (XRD, Bruker D8 Focus) with Cu K α radiation ($\lambda = 1.54056 \text{ \AA}$) at 40 kV and 40 mA . XRD spectra were collected over a 2θ range of $30\text{--}60^\circ$ at a scanning speed of $8^\circ/\text{min}$. XPS analyses of precatalysts were carried out on a Physical Electronics PHI 1600 ESCA system with an Al K α X-ray source (1486.6 eV). The binding energy was calibrated using the C 1s photoelectron peak at 284.6 eV as the reference.

In-situ Raman spectroscopy measurements. In-situ Raman spectroscopy was carried out in a custom-designed flow cell (Supplementary Fig. 12a), which was manufactured by Gaosunion Co., Ltd., Tianjin. The electrode was encased in a PEEK fitting, with an exposed circular geometric surface area of $\sim 1 \text{ cm}^2$. A platinum wire and an Ag/AgCl electrode (saturated KCl, Gaosunion Co., Ltd., Tianjin) were used as the counter and the reference electrode, respectively. The counter electrode is separated from the working electrode by an anion exchange membrane (FAA-3-PK-75, Fumatech) to avoid cross-contamination. In situ Raman spectroscopy was performed with a Raman microscopy system (LabRAM HR Evolution, Horiba Jobin Yvon). A He–Ne laser ($\lambda = 532 \text{ nm}$) served as the excitation source. All spectra were collected at a constant potential (-0.5 V versus the RHE). Electrochemical measurements were carried out with a potentiostat (CompactStat.e20250, IVIUM).

In-situ ATR-SEIRAS measurements. In-situ ATR-SEIRAS was performed with an ATR configuration. Au nanofilms were deposited directly on the reflecting plane of a Si prism using a modified electroless chemical deposition method outlined by Xu et al.⁵⁸ The spectroelectrochemical cell was based on the design of Xu et al.⁵⁹ and manufactured by Gaosunion Co., Ltd., Tianjin. In order to reduce the corrosion of Si crystal, 0.1 M KOH was used as the electrolyte. The counter electrode (a graphite rod) was separated from the working and reference electrodes, i.e., the catalyst film and a saturated Ag/AgCl electrode (saturated KCl, Gaosunion Co., Ltd., Tianjin), respectively, with a piece of anion exchange membrane (AEM, FAA-3-PK-75, Fumatech). This cell is integrated into the FTIR (is50, Nicolet) spectrometer with a modified accessory at a 60° incident angle (VeeMax III, PIKE Technology). All spectra were collected with a 4 cm^{-1} resolution. Spectra are presented in absorbance, with positive and negative peaks showing an increase and decrease in signal, respectively. As for LRS-Cu, MRS-Cu and HRS-Cu, they were deposited on the Au nanofilm coated-Si prisms like the process described above, while W-Cu was drop-casted onto the Au nanofilm coated-Si prisms. The background was taken at $+0.1 \text{ V}$ versus the RHE in Ar saturated electrolyte for each electrode. Electrochemical measurements are carried out with a potentiostat (CompactStat.e20250, IVIUM).

OH^- electroadsorption measurements. In-situ OH_{ads} studies were conducted by flowing Ar in the flow cell (Supplementary Fig. 15). First, CO_2 electrolysis was conducted at a constant potential of -0.5 V versus the RHE for 1 h by switching the gas feed to CO_2 and flowing the electrolyte. Immediately after electrolysis, the electrolyte (1 M NaOH (a.q.)) flow rate was stopped to minimize the fluctuation in the voltammogram, and the gas feed was switched to Ar, the electrolyte flow rate was stopped, and then cyclic voltammetry (20 mV/s) was performed. Electrochemical measurements are carried out with a potentiostat (Autolab PGSTAT204, Metrohm).

ECSA measurements. The ECSA was determined by measuring the double-layer capacitance (C_{DL}) of various electrodes in Ar-purged 2 M KOH (aq.) in the flow cell (Supplementary Fig. 15) and the ECSA was measured after CO_2 electrolysis at a constant potential of -0.5 V versus the RHE for 1 h . Immediately after electrolysis, the gas feed was switched to Ar, and then the electrolyte flow rate was stopped to

minimize the fluctuation in the voltammogram. The scan rate was varied from 25 to 125 mV s⁻¹ in the non-faradaic potential region and the observed current was plotted as a function of scan rate to obtain the C_{DL}. ECSA was determined by normalizing the C_{DL} to that of a Cu foil. Electrochemical measurements are carried out with a potentiostat (CHI 660E, CH Instruments Inc.).

Electrochemical reduction of CO₂ in a flow cell. CO₂ reduction was conducted in a custom-designed three-chamber flow cell manufactured by Gaossunion Co., Ltd. (Supplementary Fig. 15), where the CO₂ gas was supplied directly to the catalyst layer (cathode, working electrode). The CO₂ gas flow rate was controlled using a mass flow controller (MC-Series, Alicat Scientific) and set to 10 sccm. However, it is well known that OH⁻ can react with CO₂ to form HCO₃⁻ or CO₃²⁻. Therefore, the calculation based on the inlet CO₂ flow rate will result in overestimated F.E. results^{60,61}. For this reason, we used another flowmeter (M-Series, Alicat Scientific) to detect the CO₂ flow rate at the outlet of the reactor and used this number as the basis for calculating F.E. Aqueous KOH solution (2 M) was used as both the catholyte and the anolyte. Activated Ni foam was used as the anode (counter electrode). Peristaltic pumps (EC200-01, Gaossunion Co., Ltd.) were used to control the flow rate of the electrolytes at ~10 ml min⁻¹. An AEM (FAA-3-PK-75, Fumatech) was used to separate the cathode and anode chambers. Electrolysis experiments were conducted using chronoamperometry with a potentiostat (CompactStat.e20250, IVIUM). The cathode potentials were measured against a Hg/HgO reference electrode (1 M KOH, Gaossunion Co., Ltd., Tianjin). For each measurement, products were quantified after the amount of electron flowing through the cathode achieved 50 C and at least three replicates were conducted to obtain an average value with the standard deviation. It should be noted that iR correction was not performed.

Electrochemical reduction of CO₂ in the MEA system. The MEA cell (manufactured by Gaossunion Co., Ltd.) consists of a titanium anode (cathode) bipolar plate with serpentine flow field, associated nuts, bolts, and insulating kit. The geometric area of each flow field is 4 or 25 cm² (Supplementary Fig. 40). An AEM membrane (FAA-3-PK-75, Fumatech) was activated in 0.1 M KOH for 24 h, washed with ultra-purity water prior to use. The anode consisted of iridium oxide supported on titanium mesh (IrOx/Ti mesh) was prepared by a dip-coating and thermal decomposition method⁶². The MEA was assembled in a way as illustrated in Fig. 5a. A direct current power supply (UTP1300, UNI-T Group Co., Ltd) was used to apply current to the MEA. A Corrtest CS350M in a galvanostatic mode was used to measure the cell voltage. No iR compensation was applied. Aqueous KHCO₃ electrolyte (0.1 M) was used as the anolyte and was circulated using a peristaltic pump (EC200-01, Gaossunion Co., Ltd.). The electrolyte flow rate was kept at 10 mL min⁻¹. As the current density and electrode area increase, the CO₂ flow rate should be adjusted upwards to avoid mass transfer limitations of CO₂ while maintaining optimum selectivity. The flow rate of the CO₂ gas flowing into the cathode flow field was kept at 20 or 60 sccm by a mass flow controller (MC-Series, Alicat Scientific) for different geometries of the flow field. CO₂ was flowed through a homemade humidifier (7/8 full of Milli-Q water, room temperature) prior to the MEA. The flow rate of the CO₂ gas flowing out the cathode flow field was also measured by a flowmeter (M-Series, Alicat Scientific). The liquid products carried by CO₂ gas are absorbed by low-temperature ultra-purity water obtained from an ice salt bath.

Analysis of CO₂ reduction products. During electrolysis, gas products were quantified using an on-line gas chromatography system (GC7890B, Agilent Technologies, Inc.). The thermal conductivity detector (TCD) connected to a MolSieve 5A packed column (Agilent Technologies, Inc.) to detect H₂, O₂, and N₂ and a back flame ionization detector (FID) connected to a Porapak Q packed column (Agilent Technologies, Inc.) to detect CO. A methanizer was installed to enable the back FID to detect CO with 1000 times higher sensitivity. A front FID connected to an HP-PLOT Al₂O₃ capillary column (Agilent Technologies, Inc.) to detect hydrocarbons (C1~C3). Ar was used as the carrier gas. After passing through the reactor, the gas was allowed to flow directly into the gas sampling loop of the gas chromatography for online gaseous product analysis.

In the performance test using flow cell and the MEA system, the liquid products were collected from the cathode and anode chambers⁶⁰. The liquid products were analyzed by headspace gas chromatography (HS-GC) and ¹H-NMR. HS-GC measurements were carried out using a BChP HS-2 Headspace Sampler with GC2060 gas chromatography (Shanghai Ruimin Instrument Co., Ltd.). Typically, 10 mL vials were filled with 3 mL of the liquid sample and sealed. They were heated to 70 °C over 20 min in the headspace sampler and 1 mL of the headspace gas composition was automatically injected into the GC. The sample loop (110 °C) and transfer line (110 °C) were both heated to avoid condensation. Ar was used as the carrier gas. An HP-INNOWax capillary column (Length: 60 m; ID: 0.32 mm; Film: 0.5 μm, Agilent) was used to separate the compounds in the sample. ¹H-NMR was performed using AVANCE IITM HD 400 MHz NanoBAY. The water suppression method was used. DMSO (10 mM) and phenol (50 mM) were added as internal standards. For CO₂

reduction products showing multiple sets of NMR peaks, the set of peaks with the highest intensity were chosen for calibration and quantification.

Construction of the photovoltaic-electrolyzer (PV-EC) system. The simulated solar illumination was obtained from a 300 W Xenon arc lamp (Microsolar 300 UV, Beijing Perfectlight Technology Co. Ltd.) equipped with an air mass 1.5 global (AM 1.5G) filter, and the power intensity of the incident light was calibrated to 100 mW/cm² using a Si photodiode (FDS100, Thorlabs). The solar panel was based on five p-n⁺ Si solar cells connected in series (effective illuminated area of ~5.7 cm²). A Source Measure Unit (2450, Keithley) was wired in series with 0 V applied to monitor the current. The electrolyzer is the flow cell.

Computational methods. Vienna ab initio simulation package (VASP) was used to carry out calculations with the PBE exchange-correlation functional^{63,64}. Van der Waals interactions were accounted for by using the DFT-D3 method⁶⁵. The cut-off energy is 400 eV. The interactions between the atomic cores and electrons were described by the projector augmented wave (PAW) method⁶⁶. All structures were optimized until the force on each atom has been less than 0.02 eV/Å. The transition state search was conducted with the climbing image nudged elastic band (CI-NEB) method, followed by the dimer method to converge the saddle point within 0.05 eV/Å. We access CO dimerization on the three models. A four-layer Cu(111)-(3×3) slab with a (3×3×1) k-point grid and a four-layer Cu(100)-(3×3) slab with a (3×3×1) k-point grid were used as models for DFT calculations. The bottom two layers are fixed while the upper two layers were relaxed during optimization. One layer of water with a simple hydronium ion was chosen to simulate the electrochemical interface⁶⁷⁻⁶⁹.

Data availability

The authors declare that all data supporting the results of this study are available within the paper and its supplementary information files or from the corresponding authors upon reasonable request.

Received: 3 June 2021; Accepted: 6 September 2021;

Published online: 30 September 2021

References

- Kattel, S., Ramirez, P. J., Chen, J. G., Rodriguez, J. A. & Liu, P. Active sites for CO₂ hydrogenation to methanol on Cu/ZnO catalysts. *Science* **355**, 1296–1299 (2017).
- Dinh, C. T. et al. CO₂ electroreduction to ethylene via hydroxide-mediated copper catalysis at an abrupt interface. *Science* **360**, 783–787 (2018).
- Nitopi, S. et al. Progress and perspectives of electrochemical CO₂ reduction on copper in aqueous electrolyte. *Chem. Rev.* **119**, 7610–7672 (2019).
- Li, F. et al. Molecular tuning of CO₂-to-ethylene conversion. *Nature* **577**, 509–513 (2020).
- Yang, P. P. et al. Protecting copper oxidation state via intermediate confinement for selective CO₂ electroreduction to C₂+ fuels. *J. Am. Chem. Soc.* **142**, 6400–6408 (2020).
- Zhong, M. et al. Accelerated discovery of CO₂ electrocatalysts using active machine learning. *Nature* **581**, 178–183 (2020).
- Ma, W. C. et al. Electrocatalytic reduction of CO₂ to ethylene and ethanol through hydrogen-assisted C–C coupling over fluorine-modified copper. *Nat. Catal.* **3**, 478–487 (2020).
- Jung, H. et al. Electrochemical fragmentation of Cu₂O nanoparticles enhancing selective C–C coupling from CO₂ reduction reaction. *J. Am. Chem. Soc.* **141**, 4624–4633 (2019).
- Durand, W. J., Peterson, A. A., Studt, F., Abild-Pedersen, F. & Norskov, J. K. Structure effects on the energetics of the electrochemical reduction of CO₂ by copper surfaces. *Surf. Sci.* **605**, 1354–1359 (2011).
- Jiang, K. et al. Metal ion cycling of Cu foil for selective C–C coupling in electrochemical CO₂ reduction. *Nat. Catal.* **1**, 111–119 (2018).
- Xia, Y., Xiong, Y., Lim, B. & Skrabalak, S. E. Shape-controlled synthesis of metal nanocrystals: simple chemistry meets complex physics? *Angew. Chem. Int. Ed.* **48**, 60–103 (2009).
- Wang, Z., Yang, G., Zhang, Z., Jin, M. & Yin, Y. Selectivity on etching: creation of high-energy facets on copper nanocrystals for CO₂ electrochemical reduction. *ACS Nano* **10**, 4559–4564 (2016).
- De Gregorio, G. L. et al. Facet-dependent selectivity of Cu catalysts in electrochemical CO₂ reduction at commercially viable current densities. *ACS Catal.* **10**, 4854–4862 (2020).
- Wang, H. X. et al. Self-selective catalyst synthesis for CO₂ reduction. *Joule* **3**, 1927–1936 (2019).

15. Wang, Y. et al. Catalyst synthesis under CO₂ electroreduction favours faceting and promotes renewable fuels electrosynthesis. *Nat. Catal.* **3**, 98–106 (2019).
16. Tao, A. R., Habas, S. & Yang, P. D. Shape control of colloidal metal nanocrystals. *Small* **4**, 310–325 (2008).
17. Niu, Z. & Li, Y. Removal and utilization of capping agents in nanocatalysis. *Chem. Mater.* **26**, 72–83 (2013).
18. Hou, Y. H. et al. Photonic curing: activation and stabilization of metal membrane catalysts (MMCs) for the electrochemical reduction of CO₂. *ACS Catal.* **9**, 9518–9529 (2019).
19. Nwabara, U. O., Cofell, E. R., Verma, S., Negro, E. & Kenis, P. J. A. Durable cathodes and electrolyzers for the efficient aqueous electrochemical reduction of CO₂. *ChemSusChem* **13**, 855–875 (2020).
20. Yang H., et al. Recent progress in self-supported catalysts for CO₂ electrochemical reduction. *Small Methods* **4**, 1900826 (2020).
21. Ott, S. et al. Ionomer distribution control in porous carbon-supported catalyst layers for high-power and low Pt-loaded proton exchange membrane fuel cells. *Nat. Mater.* **19**, 77–85 (2020).
22. Zhou, Y.-G., Kang, Y. & Huang, J. Fluidized electrocatalysis. *CCS Chem.* **2**, 31–41 (2020).
23. Wei, X., Li, Y., Chen, L. & Shi, J. Formic acid electro-synthesis by concurrent cathodic CO₂ reduction and anodic CH₃OH oxidation. *Angew. Chem. Int. Ed.* **60**, 3148–3155 (2021).
24. Dobrev, D. Ion-beam-induced texture formation in vacuum-condensed thin metal films. *Thin Solid Films* **92**, 41–53 (1982).
25. Abadias, G. Stress and preferred orientation in nNitride-based PVD coatings. *Surf. Coat. Technol.* **202**, 2223–2235 (2008).
26. Lv, Y. H. et al. Influence of substrate bias voltage on structure and properties of the CrAlN films deposited by unbalanced magnetron sputtering. *Appl. Surf. Sci.* **258**, 3864–3870 (2012).
27. Zheng, J. Y., Bao, S. H., Guo, Y. & Jin, P. Anatase TiO₂ films with dominant {001} facets fabricated by direct-current reactive magnetron sputtering at room temperature: oxygen defects and enhanced visible-light photocatalytic behaviors. *ACS Appl. Mater. Interfaces* **6**, 5940–5946 (2014).
28. Li, F. et al. Cooperative CO₂-to-ethanol conversion via enriched intermediates at molecule-metal catalyst interfaces. *Nat. Catal.* **3**, 75–82 (2019).
29. Cao, L. et al. Mechanistic insights for low-overpotential electroreduction of CO₂ to CO on copper nanowires. *ACS Catal.* **7**, 8578–8587 (2017).
30. Droog, J. M. M. & Schlenter, B. Oxygen electroreduction on copper single crystal electrodes in sodium hydroxide solution. *J. Electroanal. Chem. Interfacial Electrochem.* **112**, 387–390 (1980).
31. Schouten, K. J., Qin, Z., Perez Gallent, E. & Koper, M. T. Two pathways for the formation of ethylene in CO reduction on single-crystal copper electrodes. *J. Am. Chem. Soc.* **134**, 9864–9867 (2012).
32. Lv, J. J. et al. A highly porous copper electrocatalyst for carbon dioxide reduction. *Adv. Mater.* **30**, e1803111 (2018).
33. LaGrow, A. P., Ward, M. R., Lloyd, D. C., Gai, P. L. & Boyes, E. D. Visualizing the Cu/Cu₂O interface transition in nanoparticles with environmental scanning transmission electron microscopy. *J. Am. Chem. Soc.* **139**, 179–185 (2017).
34. Feng, X., Jiang, K., Fan, S. & Kanan, M. W. Grain-boundary-dependent CO₂ electroreduction activity. *J. Am. Chem. Soc.* **137**, 4606–4609 (2015).
35. Jin, M. et al. Shape-controlled synthesis of copper nanocrystals in an aqueous solution with glucose as a reducing agent and hexadecylamine as a capping agent. *Angew. Chem. Int. Ed.* **50**, 10560–10564 (2011).
36. Wang, X., Varela, A. S., Bergmann, A., Kuhl, S. & Strasser, P. Catalyst particle density controls hydrocarbon product selectivity in CO₂ electroreduction on Cu₂O. *ChemSusChem* **10**, 4642–4649 (2017).
37. Kas, R. K. et al. Electrochemical CO₂ reduction on nanostructured metal electrodes: fact or defect? *Chem. Sci.* **11**, 1738–1749 (2020).
38. Reske, R. et al. Controlling catalytic selectivities during CO₂ electroreduction on thin Cu metal overlayers. *J. Phys. Chem. Lett.* **4**, 2410–2413 (2013).
39. Tan, Y. C., Lee, K. B., Song, H. & Oh, J. Modulating local CO₂ concentration as a general strategy for enhancing C–C coupling in CO₂ electroreduction. *Joule* **4**, 1104–1120 (2020).
40. Lee, S. H. et al. Oxidation state and surface reconstruction of Cu under CO₂ reduction conditions from in situ x-ray characterization. *J. Am. Chem. Soc.* **143**, 588–592 (2021).
41. Jouny, M., Luc, W. & Jiao, F. High-rate electroreduction of carbon monoxide to multi-carbon products. *Nat. Catal.* **1**, 748–755 (2018).
42. Heyes, J., Dunwell, M. & Xu, B. CO₂ reduction on Cu at low overpotentials with surface-enhanced in situ spectroscopy. *J. Phys. Chem. C.* **120**, 17334–17341 (2016).
43. Sartin, M. M. et al. Effect of particle shape and electrolyte cation on CO adsorption to copper oxide nanoparticle electrocatalysts. *J. Phys. Chem. C.* **122**, 26489–26498 (2018).
44. Gunathunge, C. M., Ovalle, V. J., Li, Y. W., Janik, M. J. & Waegle, M. M. Existence of an electrochemically inert CO population on Cu electrodes in alkaline pH. *ACS Catal.* **8**, 7507–7516 (2018).
45. Ren, D., Fong, J. & Yeo, B. S. The effects of currents and potentials on the selectivities of copper toward carbon dioxide electroreduction. *Nat. Commun.* **9**, 925 (2018).
46. Ren, D., Gao, J., Zakeeruddin, S. M. & Grätzel, M. New insights into the interface of electrochemical flow cells for carbon dioxide reduction to ethylene. *J. Phys. Chem. Lett.* **12**, 7583–7589 (2021).
47. Goodpaster, J. D., Bell, A. T. & Head-Gordon, M. Identification of possible pathways for C–C bond formation during electrochemical reduction of CO₂: new theoretical insights from an improved electrochemical model. *J. Phys. Chem. Lett.* **7**, 1471–1477 (2016).
48. Schreier, M., Yoon, Y., Jackson, M. N. & Surendranath, Y. Competition between H and CO for active sites governs copper-mediated electrosynthesis of hydrocarbon fuels. *Angew. Chem. Int. Ed.* **57**, 10221–10225 (2018).
49. Clark, E. L., Hahn, C., Jaramillo, T. F. & Bell, A. T. Electrochemical CO₂ reduction over compressively strained CuAg surface alloys with enhanced multi-carbon oxygenate selectivity. *J. Am. Chem. Soc.* **139**, 15848–15857 (2017).
50. Li, J. et al. Constraining CO coverage on copper promotes high-efficiency ethylene electroproduction. *Nat. Catal.* **2**, 1124–1131 (2019).
51. Malkani, A. S., Dunwell, M. & Xu, B. Operando spectroscopic investigations of copper and oxide-derived copper catalysts for electrochemical CO reduction. *ACS Catal.* **9**, 474–478 (2018).
52. Sandberg, R. B., Montoya, J. H., Chan, K. & Norskov, J. K. CO–CO coupling on Cu facets: coverage, strain, and field effects. *Surf. Sci.* **654**, 56–62 (2016).
53. Resasco, J. et al. Promoter effects of alkali metal cations on the electrochemical reduction of carbon dioxide. *J. Am. Chem. Soc.* **139**, 11277–11287 (2017).
54. Ren, D., Loo, N. W. X., Gong, L. & Yeo, B. S. Continuous production of ethylene from carbon dioxide and water using intermittent sunlight. *ACS Sustain. Chem. Eng.* **5**, 9191–9199 (2017).
55. Gao, J. et al. Selective C–C coupling in carbon dioxide electroreduction via efficient spillover of intermediates as supported by operando Raman spectroscopy. *J. Am. Chem. Soc.* **141**, 18704–18714 (2019).
56. Weng, L. C., Bell, A. T. & Weber, A. Z. Modeling gas-diffusion electrodes for CO₂ reduction. *Phys. Chem. Phys.* **20**, 16973–16984 (2018).
57. Burdyny, T. & Smith, W. A. CO₂ reduction on gas-diffusion electrodes and why catalytic performance must be assessed at commercially-relevant conditions. *Energy Environ. Sci.* **12**, 1442–1453 (2019).
58. Dunwell, M. et al. The central role of bicarbonate in the electrochemical reduction of carbon dioxide on gold. *J. Am. Chem. Soc.* **139**, 3774–3783 (2017).
59. Li, J. et al. Electrokinetic and in situ spectroscopic investigations of CO electrochemical reduction on copper. *Nat. Commun.* **12**, 3264 (2021).
60. Zhang, J., Luo, W. & Zuttel, A. Crossover of liquid products from electrochemical CO₂ reduction through gas diffusion electrode and anion exchange membrane. *J. Catal.* **385**, 140–145 (2020).
61. Ma, M. et al. Insights into the carbon balance for CO₂ electroreduction on Cu using gas diffusion electrode reactor designs. *Energy Environ. Sci.* **13**, 977–985 (2020).
62. Luc, W., Rosen, J. & Jiao, F. An Ir-based anode for a practical CO₂ electrolyzer. *Catal. Today* **288**, 79–84 (2017).
63. Kresse, G. & Hafner, J. Ab initio molecular-dynamics simulation of the liquid-metal-amorphous-semiconductor transition in germanium. *Phys. Rev. B* **49**, 14251–14269 (1994).
64. Grimme, S., Antony, J., Ehrlich, S. & Krieg, H. A consistent and accurate ab initio parametrization of density functional dispersion correction (DFT-D) for the 94 elements H–Pu. *J. Chem. Phys.* **132**, 154104 (2010).
65. Liu, S., Zong, J., Zhao, Z.-J. & Gong, J. Exploring the initial oxidation of Pt, Pt₃Ni, Pt₃Au (111) surfaces: a genetic algorithm based global optimization with density functional theory. *Green. Chem. Eng.* **1**, 56–62 (2020).
66. Kresse, G. & Joubert, D. From ultrasoft pseudopotentials to the projector augmented-wave method. *Phys. Rev. B* **59**, 1758–1775 (1999).
67. Gauthier, J. A., Dickens, C. F., Chen, L. D., Doyle, A. D. & Norskov, J. K. Solvation effects for oxygen evolution reaction catalysis on IrO₂(110). *J. Phys. Chem. C.* **121**, 11455–11463 (2017).
68. Montoya, J. H., Shi, C., Chan, K. & Norskov, J. K. Theoretical insights into a CO dimerization mechanism in CO₂ electroreduction. *J. Phys. Chem. Lett.* **6**, 2032–2037 (2015).
69. Cheng, D. et al. The nature of active sites for carbon dioxide electroreduction over oxide-derived copper catalysts. *Nat. Commun.* **12**, 395 (2021).

Acknowledgements

We acknowledge the National Key R&D Program of China (2016YFB0600901), the National Natural Science Foundation of China (22038009, 21722608, 51861125104, 2212100031), the Natural Science Foundation of Tianjin City (18JCJQC47500), and the Program of Introducing Talents of Discipline to Universities (B06006) for financial support.

Author contributions

J.L.G. supervised the project. J.L.G., T.W., G.Z., and Z.J.Z. conceptualized the project. G.Z., H.M.L., and H.G. synthesized Cu-based catalysts. G.Z., H.Y.W., J. Y., and J.Y.G. conducted the catalytic tests and the related data processing. Q.Z.W. fabricated the solar panel. Z.J.Z. and D.F.C. carried out the theoretical calculations. All the authors participate in the writing of the paper.

Competing interests

The authors declare no competing interests.

Additional information

Supplementary information The online version contains supplementary material available at <https://doi.org/10.1038/s41467-021-26053-w>.

Correspondence and requests for materials should be addressed to Tuo Wang or Jinlong Gong.

Peer review information *Nature Communications* thanks Wei An, Antonio José Martín, and the other, anonymous, reviewer(s) for their contribution to the peer review of this work.

Reprints and permission information is available at <http://www.nature.com/reprints>

Publisher's note Springer Nature remains neutral with regard to jurisdictional claims in published maps and institutional affiliations.



Open Access This article is licensed under a Creative Commons Attribution 4.0 International License, which permits use, sharing, adaptation, distribution and reproduction in any medium or format, as long as you give appropriate credit to the original author(s) and the source, provide a link to the Creative Commons license, and indicate if changes were made. The images or other third party material in this article are included in the article's Creative Commons license, unless indicated otherwise in a credit line to the material. If material is not included in the article's Creative Commons license and your intended use is not permitted by statutory regulation or exceeds the permitted use, you will need to obtain permission directly from the copyright holder. To view a copy of this license, visit <http://creativecommons.org/licenses/by/4.0/>.

© The Author(s) 2021